Quantification of Gastric Slow Wave Velocity Using Bipolar High-Resolution Recordings

Henry Han [ID], Leo K. Cheng [ID], Recep Avci [ID], *Member, IEEE*, and Niranchan Paskaranandavadivel [ID]

Abstract—Objective: **Gastric bio-electrical slow waves are, in part, responsible for coordinating motility. High-resolution (HR)** *in vivo* **recordings can be used to capture the wavefront velocity of the propagating slow waves. A standard "marking-and-grouping" approach is typically employed along with manual review. Here, a bipolar velocity estimation (BVE) method was developed, which utilized local directional information to estimate the wavefront velocity in an efficient manner.** *Methods:* **Unipolar** *in vivo* **HR recordings were used to construct bipolar recordings in different directions. Then, the local directionality of the slow wave was extracted by calculating time delay information. The accuracy of the method was verified using synthetic data and then validated with** *in vivo* **HR pig experimental recordings.** *Results:* **Against ventilator noise amplitude of 0% - 70% of the average slow wave amplitude, the direction and speed error increased from $4.4°$ and 0.9 mm/s to $8.6°$ and 1.4 mm/s. For signals added with high-frequency noise with SNR of 60 dB - 12 dB, the error increased from $8.0°$ and 1.0 mm/s to $9.8°$ and 1.2 mm/s. With experimental data, the BVE algorithm resulted in 19.2 $\pm 1.7°$ of direction error and 2.0 $\pm$ 0.2 mm/s of speed error, when compared to the standard "marking-and-grouping" method.** *Conclusion:* **Gastric slow wave wavefront velocities were estimated rapidly using the BVE algorithm with minimal errors.** *Significance:* **The BVE algorithm enables the ability to estimate wavefront velocities in HR recordings in an efficient manner.**

*Index Terms—***Bipolar recording, gastric dysrhythmias, multielectrode recordings, spatio-temporal slow waves.**

I. INTRODUCTION

GASTRIC motility is coordinated, in part, by bio-electrical events known as slow waves which are generated and propagated by a network of specialized cells called the interstitial cells of Cajal [1]. *In vivo* recordings from the surface of the stomach, utilizing unipolar and bipolar recording methods, have provided an electrophysiological understanding of slow wave activity in health and disease [2], [3]. Unipolar recordings represent both far-field and local activation, whereas bipolar recordings mainly include information on local activation [4]. Furthermore, bipolar recordings are less susceptible to noise than unipolar recordings due to subtraction of global noise [5].

Unipolar and bipolar recording methods are commonly used in bio-electrical recordings such as electrocardiography and electroencephalography. In the cardiac field, to detect the depolarization around an infarction or scar, bipolar recordings are typically utilized [6]. In addition, unipolar recordings are also used in the cardiac field to define the conduction pathways in disorders such as Wolff-Parkinson-White syndrome [7]. In electromyography (EMG) applications, unipolar and bipolar recording methods have been used to capture the electrical activity of the muscles for force generation and diagnostic utility [8], [9]. Neuromuscular disorders such as Duchenne muscle dystrophy and spinal muscle atrophy can be diagnosed by using high-resolution (HR) bipolar surface EMG techniques [10]. For control of robotic prosthesis, the estimation of force exerted requires accurate prediction, and unipolar recordings are favored over bipolar recordings. [11].

Bipolar recording methods have been utilized in the gastric field but have been limited to low channel count recordings (typically around 10 - 15 electrodes) [2], [12]. Recently, the application of HR electrode arrays to record from the surface of the gastrointestinal (GI) organ from hundreds of electrodes simultaneously has provided accurate spatio-temporal profiles of slow wave activity [13]. This technique has revealed the normal conduction system in the stomach and intestines [14], [15] and also has revealed the presence of dysrhythmic or abnormal patterns, such as ectopic pacemakers and re-entrant circuits [3], [16]. An increase in circumferential slow wave velocity and amplitude has been identified as a characteristic of dysrhythmic activity [17].

Several methods exist to quantify the *in vivo* gastric slow wave propagation velocity. The most commonly used method is the "marking-and-grouping" framework [18], where all the slow wave activation times are identified using a threshold-based algorithm, and grouped into wavefronts using a region growing algorithm followed by manual review. Methods to visualize activation times and calculate velocity were already established

in the HR cardiac mapping field and were adapted for gastric HR mapping [19], [20]. In particular the use of isochronal maps were used to observe slow wave propagation, while gastric slow wave velocities were calculated using a smoothed finite-difference approach [21]. An alternative method exists for estimating slow wave velocities by determining the time-delay between unipolar recordings via cross-correlations [22]. This approach was more efficient than the "marking-and-grouping" framework as identifying and grouping activation times can be time consuming. The local directional information from HR bipolar slow wave recordings has not been explored to-date. Cardiac bipolar recordings have shown that the signal amplitude provides information about the wavefront orientation, areas of conduction block, and presence of diseased tissue [23]. Similar advances are vital for gastric bio-electrical recordings.

In this paper, a novel bipolar velocity estimation (BVE) method was developed to detect the wavefront velocity of slow waves in HR mapping. It was applied to synthetic and experimental data and was validated against the standard "marking-and-grouping" framework.

II. METHODS

A. Experimental in Vivo Methods and Pre-Processing

Ethical approval for experimental studies was granted by the University of Auckland Animal Ethics Committee. The experimental methods and animal care were performed as previously described [24]. In brief, the pigs were anesthetized, after which a mid-line laparotomy was performed to gain access to the gastric serosal surface. HR flexible printed circuit board (FPC) electrodes (128–256 channels with 4 mm spacing) were then placed on the gastric serosa. Warm saline-soaked gauze was placed over the HR FPC electrodes, after which the wound edges were approximated. Data were recorded using a passive ActiveTwo recording system (BioSemi, Amsterdam, the Netherlands) at 512 Hz. The reference electrodes were placed on the hindquarter thigh. The pigs were euthanized at the end of the experiments while under anesthesia.

Raw experimental recordings were first down-sampled to 30 Hz. Then, baseline drift was removed by a Gaussian moving median filter, followed by a Savitzky-Golay filter to remove the high-frequency noise [25]. Pre-processing, data analysis, and method development were all performed in MATLAB R2019b (MathWorks, Natick, MA, USA).

B. Synthetic Signal Generation

Synthetic unipolar HR signals were generated using experimental unipolar slow wave recordings from in vivo pig studies. The first principal component of experimental slow wave events from one 10-min channel was defined as the noise-free slow wave signal event [26]. This event was used to define three synthetic HR data sets [27] (10×10 channels of 4 mm spacing): (i) linear wavefront pattern (oriented at $45°$), (ii) pacemaker wavefront pattern, and (iii) colliding wavefront pattern.

To mimic the presence of noise in an experimental setting, ventilator (low-frequency) and high-frequency noise were added to the synthetic slow wave signals [28]. Ventilator noise originates from the pig breathing during the experiment, and high-frequency noise is from electrical interference. In brief, simulated ventilator noise was modeled as a sine wave which ranged 0%–100% of the average slow wave amplitude, with a frequency of 12 cycles per minute (cpm). High-frequency noise was simulated as Gaussian white noise with an SNR range of 4–60 dB. For each noise type and noise level, 50 noise signals were randomly generated to evaluate the performance of the algorithm.

C. The BVE Algorithm

The flowchart of the BVE algorithm is shown in Fig. 1. The algorithm was divided into three main stages: (i) slow wave event likelihood estimation using kurtosis of the signal gradient, (ii) wavefront orientation estimation using bipolar signals, and (iii) computation of wavefront velocity using the bipolar signal morphology.

The filtered signals were segmented using a sliding window of 17 s and a step size of 1 s. To avoid two or more wavefronts in a single window, a window length of 17 s was chosen, which accounted for a normal slow wave frequency as high as 3.5 cpm in a pig stomach [24].

1) Slow Wave Event Likelihood Estimation Using Kurtosis of Signal Gradient:
To estimate if slow waves were present in the unipolar segments, two conditional criteria were to be satisfied. The first was an adaptive amplitude range threshold, followed by a kurtosis of signal gradient threshold.

The first threshold condition was based on an observation that a slow wave segment with a very high or low amplitude range was unlikely to include a slow wave event. An adaptive threshold (AdTh) of acceptable signal amplitude range was calculated for each sliding window. AdTh was defined as the range from negative to positive standard deviation (SD) from the mean amplitude range of the signal segments across all channels, as in

$$AdTh = [E(R) - \sigma, E(R) + \sigma], \qquad (1)$$

where R represents the amplitude ranges of the signal segments across all channels, $E()$ denotes the mean and σ denotes the SD of R. Any signal segment with an amplitude range within the AdTh was not likely to contain large noise deviations and was used in the next step.

During data analysis, it was observed that a signal segment with slow wave events typically had gradient values of a leptokurtic distribution, while a signal segment without slow wave events had gradient values of a mesokurtic distribution. As a result, the kurtosis of the signal gradient (KuGr) was used to quantify how likely slow wave events were recorded [29], as in

$$KuGr_{x,y} = \frac{E([S'_{x,y} - E(S'_{x,y})]^4)}{[E([S'_{x,y} - E(S'_{x,y})]^2)]^2}, \qquad (2)$$

where $KuGr_{x,y}$ denotes the KuGr of the signal segment from a channel with the coordinates of (x, y) in the electrode array, and $S'_{x,y}$ denotes the gradient of the signal segment of this channel.

After empirical testing with experimental data, a KuGr value of 20 was selected as the threshold. Two examples of KuGr
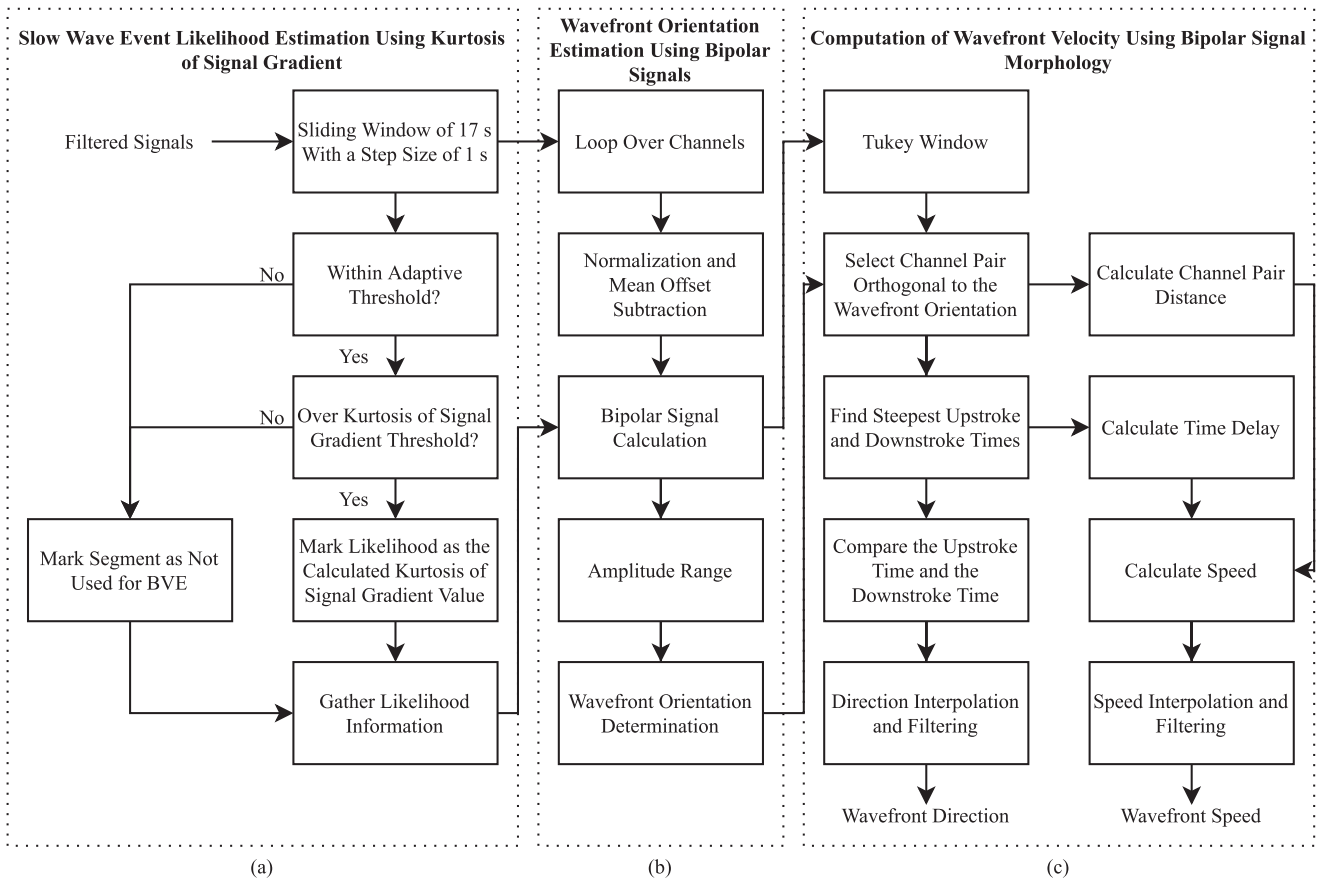
Fig. 1. Flowchart of the BVE algorithm. The algorithm was divided into three main stages: (a) slow wave event likelihood estimation using kurtosis of the signal gradient, (b) wavefront orientation estimation using bipolar signals, and (c) computation of wavefront velocity using the bipolar signal morphology.
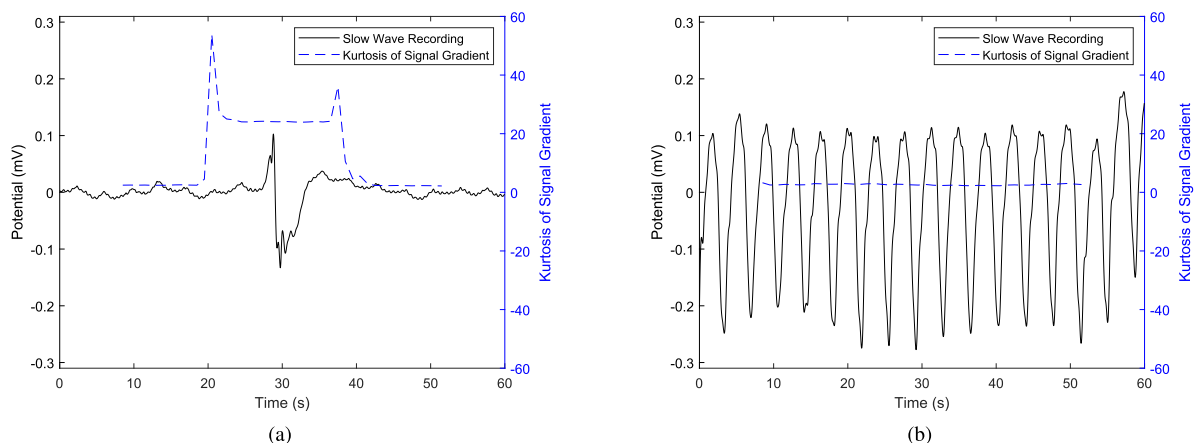

Fig. 2. Examples of running kurtosis of signal gradient calculation for experimental recordings: (a) a slow wave signal, and (b) a noisy recording with ventilation artifacts. Kurtosis of the signal gradient was calculated on a moving window of 17 s.

calculation of experimental recordings are shown in Fig. 2. When a slow wave event was present in the segment, the KuGr value was over 20 (Fig. 2(a)). However, when a slow wave event was not present, the KuGr value was below 20 (Fig. 2(b)). In the BVE algorithm, if KuGr was over the threshold, it was considered to have a high likelihood of containing a slow wave

event, and was considered for further processing. Otherwise, the signal segment was excluded for further processing.

2) Wavefront Orientation Estimation Using Bipolar Signals: If electrodes were located along a wavefront, they would have similar potential values and therefore the bipolar signal would have a relatively small amplitude, especially when
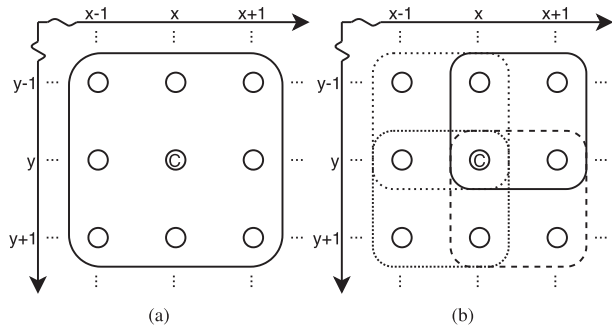
Fig. 3. Patch size configurations for the BVE algorithm. The middle channel marked with C represents the current channel with coordinates (x,y). (a) For the 3 × 3 patch configuration, there was one patch around the current channel. (b) For the 2 × 2 patch configuration, there were four possible patches around the current channel (identified by different line styles).
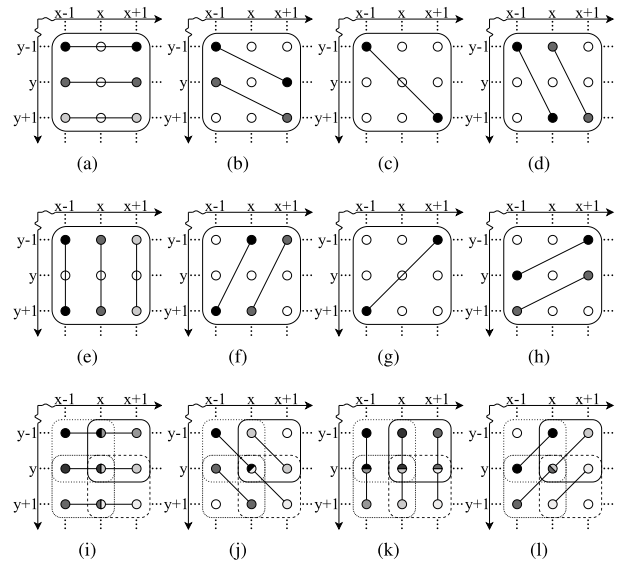

Fig. 4. Electrode pair configurations. Each figure represents the electrode pair configuration for the bipolar signal calculation of one direction. Within each figure, different colors represent different electrode pair candidates. The electrode pair with the largest total KuGr was selected as the pair to represent each direction. Eight and four directional bipolar signal segments were calculated using the electrode pairs as in (a)–(h) for the 3 × 3 patch and in (i) - (l) for the 2 × 2 patch respectively.

compared to bipolar electrode pairs oriented perpendicular to the traveling wavefront plane [23].

Signal segments were normalized to have an amplitude range of 0 - 1, after which the mean baseline offset of the normalized signal segment was subtracted. To find the wavefront orientation, bipolar signal segments of various configurations were constructed. To maintain spatial resolution and provide sufficient angle resolution, two patch sizes were selected: 3 × 3 electrodes (Fig. 3(a)) and 2 × 2 electrodes (Fig. 3(b)). Patches were translated over the electrode array sequentially. The middle channel of the patch was termed the current channel. The electrode pair configurations were designed to have distances as equal as possible to avoid bias in the amplitude range calculation.

There was always one 3 × 3 patch around the current channel. Eight directional bipolar signal segments were calculated using the signal segments of the channels within this patch with directions of 0°, 27°, 45°, 63°, 90°, 117°, 135°, and 153° (angles were reported clockwise to the positive direction of the x axis) as shown in Fig. 4(a)–(h). The electrode pair with the largest total KuGr was selected as the pair to represent each direction. If any of the eight directional bipolar signal segments was not present, the algorithm processed the current channel with a 2 × 2 patch instead.

There were at most four 2 × 2 patches around the current channel (Fig. 4(i)–(l)). Four bipolar signal segments of different directions were calculated using the signal segments of the channels within these patches (0°, 45°, 90°, and 135°). As with the 3 × 3 patch, the bipolar electrode pair in the 2 × 2 configuration with the largest total KuGr was selected to represent the direction. Directional bipolar signal segments were calculated using available patches at the edges or the corners of the electrode array. All four directional bipolar signal segments were required to compute the wavefront orientation, otherwise the orientation was unable to be estimated.

The direction of the bipolar signal segment with the smallest potential amplitude range was considered to be aligned with the wavefront.

3) Computation of Wavefront Velocity Using Bipolar Signal Morphology:
Once the wavefront orientation was determined, the algorithm assessed the morphology of the directional bipolar signal segment orthogonal to the wavefront, to estimate the propagation direction and speed. The time delay between the unipolar signal downstrokes (activation phase) of the corresponding channel pair resulted in a positive or negative deflection in the bipolar signal segment (Fig. 6(c)–(d)). To determine if it was a positive or negative deflection, a Tukey window of amplitude 1 - 2 was first applied to the bipolar signal segment to minimize boundary effects.

The gradient of the bipolar signal segment was then calculated using central finite differences, after which the steepest upstroke and downstroke points were identified. Based on this information, one of the two potential propagation directions was eliminated, resulting in the final estimated direction of the propagation. The time delay between the steepest upstroke and downstroke points was calculated from the gradient of the bipolar signal segment. The estimated speed was computed by dividing the distance between the corresponding electrode pair by the time delay.

If the slow wave frequency was higher than 3.5 cpm, two events would be present in a bipolar signal segment. In such cases, a reversed propagation velocity may be estimated, when the upstroke and downstroke points from different wavefronts were identified. Thus, a threshold of 2 s was applied on the time delay between the upstroke and downstroke points to address this issue. The threshold value of 2 s was selected to account for normal slow wave speed as low as 5.7 mm/s [24]. If the time delay was greater than the threshold, the morphology analysis would be performed again on the first half of the bipolar signal segment to account for only the first event.

After the calculation of the directions and speeds, interpolation and filtering were introduced to improve the coverage and visualization. Inverse distance weighting interpolation with a
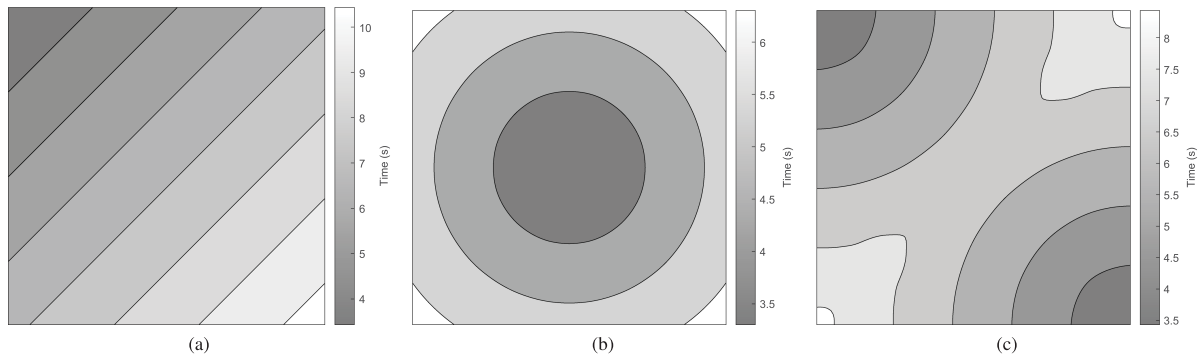
Fig. 5. Activation maps of the 3 synthetically generated slow wave profiles (isochronal level is 1 s): (a) linear wavefront, (b) pacemaker activity, and (c) colliding wavefronts.
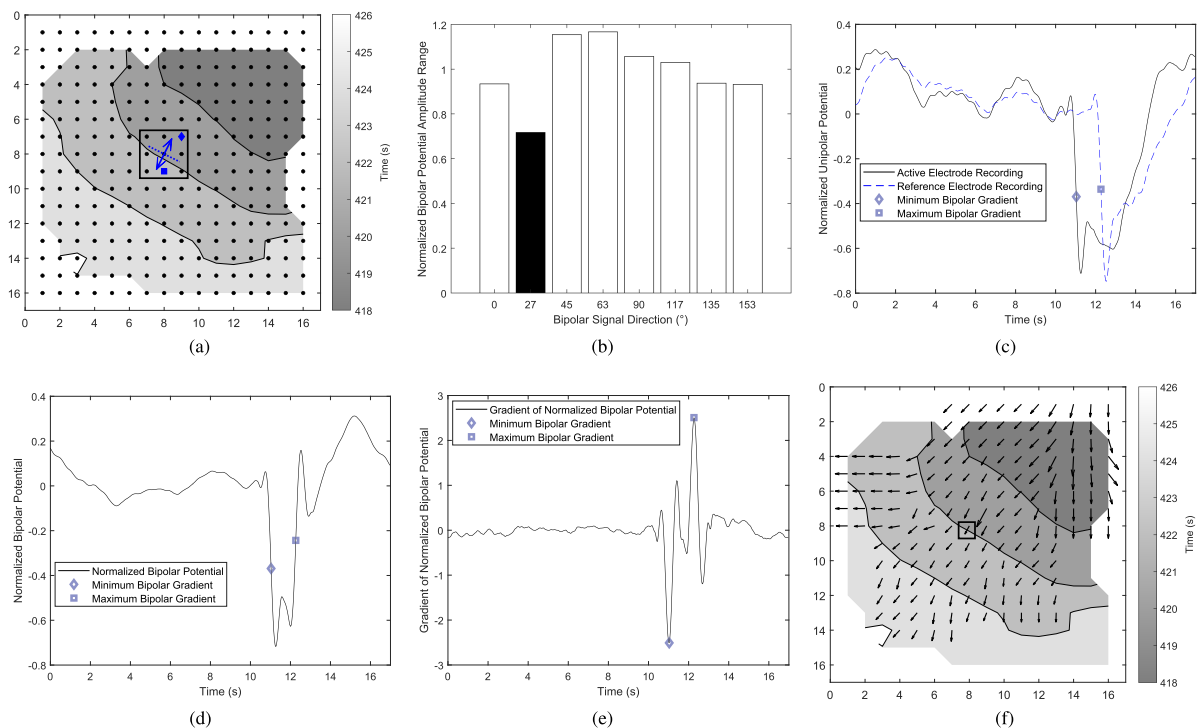

Fig. 6. Intermediate results of the BVE algorithm (isochronal level is 2 s). (a) The configuration of the HR electrode array overlaid on the activation map. The 3 × 3 square shows the patch configuration. The dotted line shows the estimated wavefront orientation. The two potential propagation directions are shown as arrows. The blue diamond and square show the locations of the active and the reference electrodes in (c). (b) The normalized bipolar potential amplitude range of the eight directional bipolar segments. The solid bar shows the smallest range. (c) The unipolar signal segments from the electrode pair that was orthogonal to the estimated wavefront. (d) The bipolar signal segment corresponding to (c). (e) The gradient of (d). (f) The interpolated and filtered velocity estimation overlaid on the activation map. The result for the current channel is surrounded by a square.

radius of double the inter-electrode spacing (8 mm) was applied on the estimated directions and speeds, once to interpolate, followed by once to extrapolate the edges [30]. Then, the interpolated directions and speeds were filtered with a 2-D Gaussian smoothing kernel with an SD of 0.5 [31].

D. Visualization and Performance Measurements

For the synthetic signals, the activation times were analytically defined at a frequency of 3 cpm using methods as previously described [21]. For experimental signals, the standard "marking-and-grouping" framework was applied to identify and group the activation times followed by manual review and correction [18]. For each propagating wavefront, an isochronal map was generated. The isochronal color bands indicated the area of the wavefront propagation over a given time interval. The slow wave propagation velocities were estimated using the smoothed finite difference method [21], which was used as the gold-standard.

The BVE algorithm was applied to both the synthetic and experimental signals to estimate the wavefront velocity. The velocity vectors estimated by the BVE algorithm were overlaid

as arrows on the isochronal activation maps to visualize and validate the results at each channel and for each sliding window. The angle of the arrow indicates the direction, while the length indicates the speed.

The mean absolute direction and speed errors between the velocities from the BVE algorithm and the gold-standard were computed for each sliding window with slow wave event. For the synthetic signals, the mean absolute direction and speed error against each type and level of the simulated noise was calculated for each slow wave pattern. For the experimental signals, the mean absolute direction and speed error for each pig was calculated. The overall accuracy of the BVE algorithm was measured by computing the mean absolute direction and speed error across all the pigs and reported as mean $\pm$ standard error of the mean. The time used by the "marking-and-grouping" method and the BVE algorithm was measured and compared.

III. RESULTS

Synthetic signals of the 3 propagation patterns were generated and the corresponding isochronal activation maps are shown in Fig. 5. Ten *in vivo* HR recordings, from 7 pigs (43 ± 11 kg), with a duration of 5 minutes per recording were used for this study. Four of the 10 recordings had normal slow wave patterns, while the other 6 exhibited dysrhythmic patterns.

A. The BVE Algorithm

The BVE algorithm was applied to synthetic signals and *in vivo* HR slow wave recordings. Examples of intermediate results from each stage of the algorithm and the overall results are described in the following sections.

1) Wavefront Orientation Estimation Using Bipolar Signals: An example of wavefront orientation estimation is shown in Fig. 6(a)–(b). Eight directional bipolar signal segments were constructed using the unipolar signal segments from the channels within the 3×3 patch as shown in Fig. 6(a). The potential amplitude ranges were calculated (Fig. 6(b)). The bipolar signal segment of the smallest potential amplitude range was at an orientation of $27°$, which was the estimated wavefront orientation. Two potential wavefront directions were identified at $117°$ and $297°$, which were orthogonal to the estimated wavefront (Fig. 6(a)).

2) Computation of Wavefront Velocity Using Bipolar Signal Morphology: The gradient of the bipolar signal segment that was orthogonal to the estimated wavefront was calculated, which was at $117°$ (or $297°$). The unipolar signal segments from the corresponding electrode pair are shown in Fig. 6(c). The resulting bipolar signal segment is shown in Fig. 6(d) and the gradient of the bipolar signal segment is shown in Fig. 6(e). The maximum and minimum points of the gradient of the bipolar signal segment were identified. The morphology of the deflection caused by the time delay between the unipolar signal downstrokes was analyzed. In this example, the minimum point occurred prior to the maximum point and therefore the deflection was identified as negative. Thus, the wavefront reached the active electrode before the reference electrode and the slow wave propagation direction was estimated to be $117°$.

TABLE I
MEAN ABSOLUTE DIRECTION AND SPEED ERRORS FOR SYNTHETIC SIGNALS FOR FOUR NOISE LEVELS

Noise Type	Linear	Pacemaker	Colliding	Overall
Ventilator Noise (0%)	$0°$ 0.04 mm/s	$5.3°$ 0.8 mm/s	$8.0°$ 1.8 mm/s	$4.4°$ 0.9 mm/s
Ventilator Noise (70%)	$0°$ 0.01 mm/s	$7.5°$ 1.2 mm/s	$18.2°$ 3.1 mm/s	$8.6°$ 1.4 mm/s
High-Frequency Noise (60 dB)	$0°$ 0.04 mm/s	$9.4°$ 1.0 mm/s	$14.5°$ 2.0 mm/s	$8.0°$ 1.0 mm/s
High-Frequency Noise (12 dB)	$0.1°$ 0.2 mm/s	$10.5°$ 1.1 mm/s	$18.7°$ 2.3 mm/s	$9.8°$ 1.2 mm/s

The bipolar signal segment that was orthogonal to the estimated wavefront was produced by a pair of electrodes with a distance of about 8.9 mm (Fig. 6(a)), given the inter-electrode distance was 4 mm. The time delay between the slow wave events from this pair of electrodes was 1.2 s and therefore resulted in an estimated speed of 7.4 mm/s.

B. Visualization

Fig. 6(f) shows an isochronal map using the "marking-and-grouping" approach along with the velocities from the BVE algorithm with a sliding window which ended at 427 s. The velocities were shown as arrows overlaid on the "marking-and-grouping" generated isochronal activation map. The directions of the arrows were consistent with the isochronal activation map (Fig. 6(f)).

C. Performance Measurements

1) Synthetic Signals: The mean absolute direction and speed errors at all noise levels for each slow wave pattern are shown in Fig. 7(a)–(d) and Table I.

In general, for both types of synthetic noise, the mean absolute errors increased when the SNR decreased. The linear wavefront pattern was oriented at $45°$, which matched the axis of the bipolar electrodes. Therefore, the BVE algorithm was able to accurately estimate the velocity with minimal error. Thus, the linear wavefront pattern had negligible direction and speed error for all levels of noise investigated. The pacemaker wavefront pattern showed larger errors, while the colliding wavefront pattern showed the largest errors. For the synthetic ventilator noise added signals (Fig. 7(a)–(b)), the slow wave propagation velocities of the signals became undetectable with a ventilator noise amplitude greater than 75% of the average slow wave amplitude. For the synthetic high-frequency noise added signals (Fig. 7(c)–(d)), the signals became indistinguishable at SNR lower than 12 dB (example tracings are shown in Supplementary Material). Thus, the SNRs between 60 dB and 12 dB were included in the calculations.

2) Experimental Signals: The mean absolute direction and speed errors for each pig are shown in Fig. 7(e)–(f). Pig 2 had the largest deviation as it was a case where the FPC electrode array did not have sufficient contact with the tissue. Pigs 1, 3, 4, and 5 exhibited dysrhythmic slow waves, which generally showed larger deviations than the normal slow wave activity (Pigs 6 and
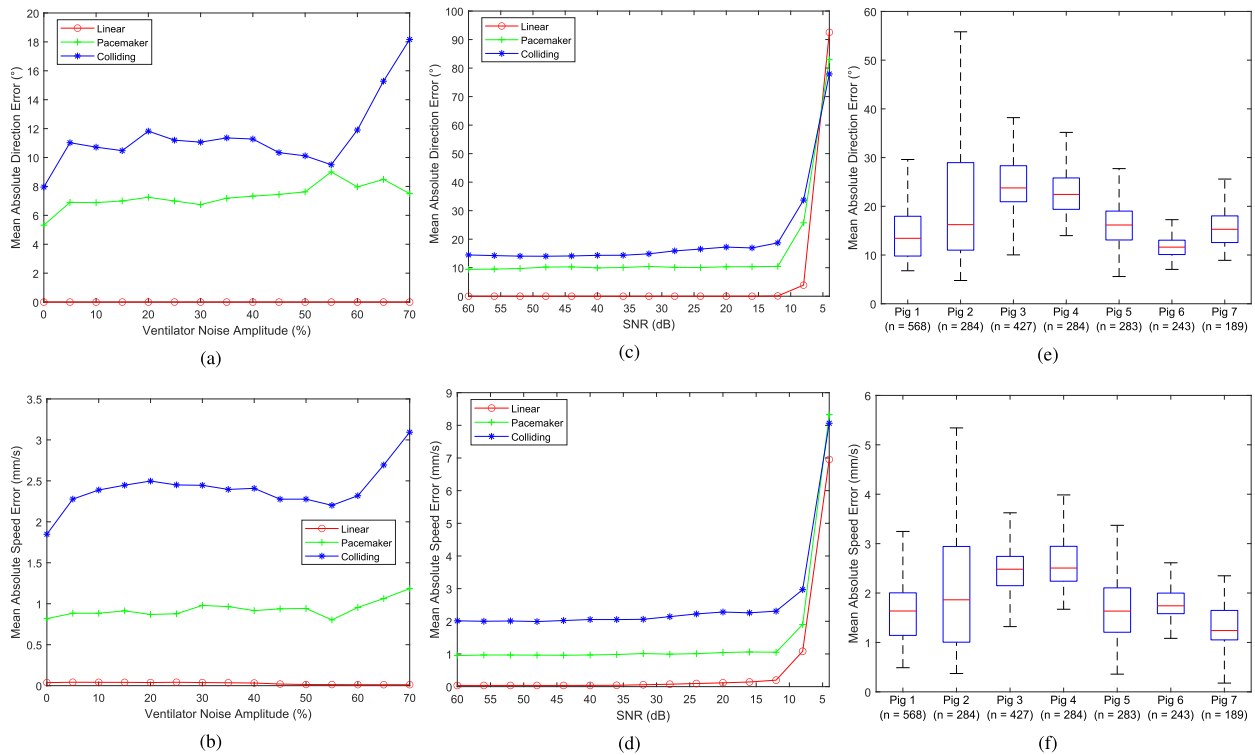
Fig. 7. Absolute direction and speed error results in comparison to the gold-standard. (a) - (b) The error results against synthetic ventilator noise. The mean error increased from 4.4° and 0.9 mm/s (0%) to 8.6° and 1.4 mm/s (70%). (c) - (d) The error results against synthetic high-frequency noise. The mean error increased from 8.0° and 1.0 mm/s (60 dB) to 9.8° and 1.2 mm/s (12 dB). Note that the amplitude of the high-frequency noise ranged from 0.2% (60 dB) to 146.4% (4 dB) of the average slow wave amplitude. (e) - (f) The error results against experimental recordings. The number of sliding windows measured for each pig is shown as n. The mean errors across all the pigs were 19.2 ± 1.7° and 2.0 ± 0.2 mm/s.

7). The mean absolute direction and speed errors across all the pigs were 19.2 ± 1.7° and 2.0 ± 0.2 mm/s.

To process a 5 minute HR (256 channels) slow wave recording, the "marking-and-grouping" method took 4 minutes without manual review and correction. This time increased to over 1 h by introducing manual review and correction to ensure the accuracy for normal slow wave propagation patterns. For dysrhythmic and dynamic slow wave propagation profiles, which included conduction blocks and ectopic pacemakers, a much longer time was required for review. However, the BVE algorithm processed the same data set in 8.7 ± 1.9 s (mean ± SD).

IV. DISCUSSION

In this paper we developed the BVE algorithm, verified the approach with with synthetic signals and validated it against the standard "marking-and-grouping" framework using *in vivo* HR experimental slow wave recordings. In the BVE algorithm, bipolar signals were constructed from HR unipolar recordings to compute the local directional information of the propagating wavefront. Gastric slow wave velocities were estimated rapidly using the BVE algorithm with minimal errors, from all the synthetic and experimental signals.

Bipolar signals have not been used in GI *in vivo* HR recordings and more information could be gained using this approach. In particular, the BVE algorithm can be used to detect regions of high velocity in gastric HR recordings, which could help identify the presence of dysrhythmias in a rapid manner [17]. The automated nature of the BVE algorithm will be significant for long term studies and chronic recordings, which are necessary to relate symptoms and GI function to bio-electrical slow wave activity [32], [33]. Bipolar slow wave recordings will also motivate new HR bipolar electrode array designs, such as electrode arrays with non-uniform density [34], [35]. There has been increasing interest to measure bio-electrical activities on the body surface and surface laplacian techniques have been commonly used to enhance the signal [36]. This method could be translated into a custom hardware electrode array as has been designed for surface electrocardiology and electroenterogram [37], [38].

In comparison to the cross-correlation velocity method [22], the BVE velocity error was higher (by 1 mm/s, 19°), but was three times more computationally efficient. In the BVE algorithm the KuGr of the unipolar recording was used as a metric to denote the likelihood of containing slow wave events, which is a novel metric that can assist with bad channel and slow wave event detection. This is similar to the application of kurtosis to assess signal fidelity for gastric slow wave analysis in real time [39].

Additional features could be incorporated to implement the BVE algorithm in real time. For example, causal linear filters can be used to enable real time processing and visualization [40]. By extending the algorithm with the ability to group and classify the estimated velocities, diseased tissue location or the orientation of muscle activation around the organ axis could be detected in real

time. New techniques such as the cardiac omnipolar mapping technique can be translated for GI applications, benefiting the BVE algorithm to provide more accurate detection results [41]. The BVE method focuses exclusively on the activation phase to estimate wavefront velocities. In future, the velocity of the slow wave recovery phase wavefront will also be computed. It is anticipated that the dispersion in the activation and recovery wavefront could play a role in the mechanisms of dysrhythmias [42].

During the third stage of the BVE algorithm (computation of wavefront velocity using bipolar signal morphology), the algorithm may not be able to estimate a velocity. This occurs when part of a slow wave event is contained in a sliding window and the maximum and minimum gradient points may not represent the deflection caused by the time delay between the downstrokes of the unipolar signal segments. In these cases, the algorithm would result in an incorrectly estimated velocity. A range of SNRs from 4.23 - 24 dB have been reported by studies using FPC electrode arrays [43], [44]. Low SNR values could occur due to technical faults and/or physiological aspects. An example of a technical fault is when the connector is not soldered correctly, and a physiological aspect is when slow waves are colliding or if there is a conduction block in the tissue. The signals in that particular region of the electrode array will have poorer SNR.

In future studies, *in vivo* experimental recordings from different species and different parts of the GI system, such as the intestine and the colon, will be used to validate the BVE algorithm. The parameters will need to be adapted for the varying frequencies and velocities for each of the GI organs. In particular, the sliding window size, the kurtosis signal gradient threshold condition, and the time difference threshold will need to be optimized.

V. CONCLUSION

A novel BVE algorithm was developed and validated to estimate the gastric slow wave propagation velocity. A key advantage of this method is that it can rapidly estimate slow wave propagation velocities, enabling real time assessment of propagation dynamics. Application of BVE during or after an intervention such as pacing [45] or ablation [46] will allow for wavefronts of interest to be rapidly determined and could aid in our understanding of slow waves in health and disease.

ACKNOWLEDGMENT

REFERENCES

[1] J. D. Huizinga, "II. Gastric motility: Lessons from mutant mice on slow waves and innervation," *Amer. J. Physiol. Gastrointest. Liver Physiol.*, vol. 281, no. 5, pp. G1129–G1134, 2001.

[2] J. Chen, B. D. Schirmer, and R. W. McCallum, "Serosal and cutaneous recordings of gastric myoelectrical activity in patients with gastroparesis," *Amer. J. Physiol. Gastrointest. Liver Physiol.*, vol. 266, no. 1, pp. G 90–G98, 1994.

[3] G. O'Grady, *et al.*, "Abnormal initiation and conduction of slow-wave activity in gastroparesis, defined by high-resolution electrical mapping," *Gastroenterology*, vol. 143, no. 3, pp. 589–598, 2012.

[4] J. M. de Bakker, "Electrogram recording and analyzing techniques to optimize selection of target sites for ablation of cardiac arrhythmias," *Pacing Clin. Electrophysiol.*, vol. 42, no. 12, pp. 1503–1516, 2019.

[5] V. DeCaprio, P. Hurzeler, and S. Furman, "A comparison of unipolar and bipolar electrograms for cardiac pacemaker sensing." *Circulation*, vol. 56, no. 5, pp. 750–755, 1977.

[6] U. B. Tedrow and W. G. Stevenson, "Recording and interpreting unipolar electrograms to guide catheter ablation," *Heart Rhythm*, vol. 8, no. 5, pp. 791–796, 2011.

[7] M. P. Nash, *et al.*, "Whole heart action potential duration restitution properties in cardiac patients: A combined clinical and modelling study," *Exp. Physiol.*, vol. 91, no. 2, pp. 339–354, 2006.

[8] J. Lara, N. Paskaranandavadivel, and L. K. Cheng, "Effect of segmentation parameters on classification accuracy of high-density EMG recordings," in *Proc. Annu. Int. Conf. IEEE Eng. Med. Biol. Soc.*, 2019, pp. 6229–6232.

[9] T. W. Beck, *et al.*, "A comparison of monopolar and bipolar recording techniques for examining the patterns of responses for electromyographic amplitude and mean power frequency versus isometric torque for the vastus lateralis muscle," *J. Neurosci. Methods*, vol. 166, no. 2, pp. 159–167, 2007.

[10] G. Rau and C. Disselhorst-Klug, "Principles of high-spatial-resolution surface EMG (HSR-EMG): Single motor unit detection and application in the diagnosis of neuromuscular disorders," *J. Electromyogr. Kinesiol.*, vol. 7, no. 4, pp. 233–239, 1997.

[11] D. A. Gabriel, "Effects of monopolar and bipolar electrode configurations on surface EMG spike analysis," *Med. Eng. Phys.*, vol. 33, no. 9, pp. 1079–1085, 2011.

[12] M. P. Mintchev, S. J. Otto, and K. L. Bowes, "Electrogastrography can recognize gastric electrical uncoupling in dogs," *Gastroenterology*, vol. 112, no. 6, pp. 2006–2011, 1997.

[13] W. Lammers, A. Al Kais, S. Singh, K. Arafat, and T. Y. el Sharkawy, "Multielectrode mapping of slow-wave activity in the isolated rabbit duodenum," *J. Appl. Physiol.*, vol. 74, no. 3, pp. 1454–1461, 1993.

[14] G. O'Grady, *et al.*, "Origin and propagation of human gastric slow-wave activity defined by high-resolution mapping," *Amer. J. Physiol. Gastrointest. Liver Physiol.*, vol. 299, no. 3, pp. G 585–G592, 2010.

[15] A. Cherian Abraham, L. K. Cheng, T. R. Angeli, S. Alighaleh, and N. Paskaranandavadivel, "Dynamic slow-wave interactions in the rabbit small intestine defined using high-resolution mapping," *Neurogastroenterol. Motil.*, vol. 31, no. 9, pp. 1–10, 2019.

[16] T. R. Angeli, *et al.*, "Circumferential and functional re-entry of in vivo slow-wave activity in the porcine small intestine," *Neurogastroenterol. Motil.*, vol. 25, no. 5, pp. e 304–e314, 2013.

[17] G. O'Grady, *et al.*, "Rapid high-amplitude circumferential slow wave propagation during normal gastric pacemaking and dysrhythmias," *Neurogastroenterol. Motil.*, vol. 24, no. 7, pp. e 299–e312, 2012.

[18] R. Yassi, *et al.*, "The gastrointestinal electrical mapping suite (GEMS): Software for analyzing and visualizing high-resolution (multi-electrode) recordings in spatiotemporal detail," *BMC Gastroenterol.*, vol. 12, no. 1, pp. 1–14, 2012.

[19] R. E. Ideker, *et al.*, "The assumptions of isochronal cardiac mapping," *Pacing Clin. Electrophysiol.*, vol. 12, no. 3, pp. 456–478, 1989.

[20] P. V. Bayly, B. H. KenKnight, J. M. Rogers, R. E. Hillsley, R. E. Ideker, and W. M. Smith, "Estimation of conduction velocity vector fields from epicardial mapping data," *IEEE Trans. Biomed. Eng.*, vol. 45, no. 5, pp. 563–571, May 1998.

[21] N. Paskaranandavadivel, G. O'Grady, P. Du, A. J. Pullan, and L. K. Cheng, "An improved method for the estimation and visualization of velocity fields from gastric high-resolution electrical mapping," *IEEE Trans. Biomed. Eng.*, vol. 59, no. 3, pp. 882–889, Mar. 2012.

[22] N. Paskaranandavadivel, G. O'Grady, and L. K. Cheng, "Time-delay mapping of high-resolution gastric slow-wave activity," *IEEE Trans. Biomed. Eng.*, vol. 64, no. 1, pp. 166–172, Jan. 2017.

[23] G. Ndrepepa, E. B. Caref, H. Yin, N. El-Sherif, and M. Restivo, "Activation time determination by high-resolution unipolar and bipolar extracellular electrograms in the canine heart," *J. Cardiovasc. Electrophysiol.*, vol. 6, no. 3, pp. 174–188, 1995.

[24] J. Egbuji, *et al.*, "Origin, propagation and regional characteristics of porcine gastric slow wave activity determined by high-resolution mapping," *Neurogastroenterol. Motil.*, vol. 22, no. 10, pp. e292–e300, 2010.

[25] N. Paskaranandavadivel, G. O'Grady, P. Du, and L. K. Cheng, "Comparison of filtering methods for extracellular gastric slow wave recordings," *Neurogastroenterol. Motil.*, vol. 25, no. 1, pp. 79–83, 2013.

[26] N. Paskaranandavadivel, L. K. Cheng, P. Du, G. O'Grady, and A. J. Pullan, "Improved signal processing techniques for the analysis of high resolution serosal slow wave activity in the stomach," in *Proc. Annu. Int. Conf. IEEE Eng. Med. Biol. Soc.*, 2011, pp. 1737–1740.

[27] H. Han, L. K. Cheng, R. Avci, and N. Paskaranandavadivel, "Detection of slow wave propagation direction using bipolar high-resolution recordings," in *Proc. Annu. Int. Conf. IEEE Eng. Med. Biol. Soc.*, 2020, pp. 837–840.

[28] H. Han, L. K. Cheng, T. R. Angeli, and N. Paskaranandavadivel, "Detection of monophasic slow-wave activation phase using wavelet decomposition," in *Proc. Annu. Int. Conf. IEEE Eng. Med. Biol. Soc.*, 2019, pp. 7157–7160.

[29] P. H. Westfall, "Kurtosis as peakedness, 1905–2014. RIP," *Amer. Stat.*, vol. 68, no. 3, pp. 191–195, 2014.

[30] D. Shepard, "A two-dimensional interpolation function for irregularly-spaced data," in *Proc. 23rd Nat. Conf. ACM*, 1968, pp. 517–524.

[31] R. C. Gonzalez, R. E. Woods, and S. L. Eddins, *Digital Image Processing Using MATLAB*. Upper Saddle River, NJ, USA: Pearson/Prentice Hall, pp. 99–107, 2004.

[32] N. Paskaranandavadivel, *et al.*, "Multi-day, multi-sensor ambulatory monitoring of gastric electrical activity," *Physiol. Meas.*, vol. 40, no. 2, pp. 1–8, 2019.

[33] L. Ver Donck, *et al.*, "Mapping slow waves and spikes in chronically instrumented conscious dogs: Implantation techniques and recordings," *Med. Biol. Eng. Comput.*, vol. 44, no. 3, pp. 170–178, 2006.

[34] S. Mansour, D. Devedeux, G. Germain, C. Marque, and J. Duchêne, "Uterine EMG spectral analysis and relationship to mechanical activity in pregnant monkeys," *Med. Biol. Eng. Comput.*, vol. 34, no. 2, pp. 115–121, 1996.

[35] M. J. Schalij, F. P. van Rugge, M. Siezenga, and E. T. van der Velde, "Endocardial activation mapping of ventricular tachycardia in patients: First application of a 32-site bipolar mapping electrode catheter," *Circulation*, vol. 98, no. 20, pp. 2168–2179, 1998.

[36] A. A. Gharibans, S. Kim, D. C. Kunkel, and T. P. Coleman, "High-resolution electrogastrogram: A novel, noninvasive method for determining gastric slow-wave direction and speed," *IEEE Trans. Biomed. Eng.*, vol. 64, no. 4, pp. 807–815, Apr. 2017.

[37] W. Besio, R. Aakula, K. Koka, and W. Dai, "Development of a tri-polar concentric ring electrode for acquiring accurate Laplacian body surface potentials," *Ann. Biomed. Eng.*, vol. 34, no. 3, pp. 426–435, 2006.

[38] J. Garcia-Casado, V. Zena-Gimenez, G. Prats-Boluda, and Y. Ye-Lin, "Enhancement of non-invasive recording of electroenterogram by means of a flexible array of concentric ring electrodes," *Ann. Biomed. Eng.*, vol. 42, no. 3, pp. 651–660, 2014.

[39] S. H. Bull, G. O'Grady, P. Du, and L. K. Cheng, "A system and method for online high-resolution mapping of gastric slow-wave activity," *IEEE Trans. Biomed. Eng.*, vol. 61, no. 11, pp. 2679–2687, Nov. 2014.

[40] S.-Y. Chen, Y. Wang, C.-C. Wu, C. Liu, and C.-I. Chang, "Real-time causal processing of anomaly detection for hyperspectral imagery," *IEEE Trans. Aerosp. Electron. Syst.*, vol. 50, no. 2, pp. 1511–1534, Apr. 2014.

[41] S. Massé, *et al.*, "Resolving myocardial activation with novel omnipolar electrograms," *Circ.: Arrhythmia Electrophysiol.*, vol. 9, no. 7, pp. 1–13, 2016.

[42] N. Paskaranandavadivel, L. K. Cheng, P. Du, J. M. Rogers, and G. O'Grady, "High-resolution mapping of gastric slow-wave recovery profiles: Biophysical model, methodology, and demonstration of applications," *Amer. J. Physiol. Gastrointest. Liver Physiol.*, vol. 313, no. 3, pp. G265–G276, 2017.

[43] N. Paskaranandavadivel, S. Alighaleh, P. Du, G. O'Grady, and L. K. Cheng, "Suppression of ventilation artifacts for gastrointestinal slow wave recordings," in *Proc. Annu. Int. Conf. IEEE Eng. Med. Biol. Soc.*, 2017, pp. 2769–2772.

[44] J. C. Erickson, *et al.*, "Intsy: A low-cost, open-source, wireless multi-channel bioamplifier system," *Physiol. Meas.*, vol. 39, no. 3, pp. 1–12, 2018.

[45] S. Alighaleh, *et al.*, "A novel gastric pacing device to modulate slow waves and assessment by high-resolution mapping," *IEEE Trans. Biomed. Eng.*, vol. 66, no. 10, pp. 2823–2830, Oct. 2019.

[46] Z. Aghababaie, *et al.*, "Feasibility of high-resolution electrical mapping for characterizing conduction blocks created by gastric ablation," in *Proc. Annu. Int. Conf. IEEE Eng. Med. Biol. Soc.*, 2019, pp. 170–173.